

He-atom diffraction from nanostructure transmission gratings: The role of imperfections

R. E. Grisenti, W. Schöllkopf, and J. P. Toennies

Max-Planck-Institut für Strömungsforschung, Bunsenstr. 10, 37073 Göttingen, Germany

J. R. Manson

Department of Physics and Astronomy, Clemson University, Clemson, South Carolina 29634

T. A. Savas and Henry I. Smith

Massachusetts Institute of Technology, Cambridge, Massachusetts 02139

(Received 2 March 1999; revised manuscript received 12 July 1999; published 15 February 2000)

The relative diffraction peak intensities of He atoms with an incident beam energy of 65 meV diffracted from a microfabricated 100 nm-period transmission grating are analyzed using both Fresnel and Fraunhofer diffraction theory. The projected slit width could be varied from 50 nm down to less than 1 nm by inclining the grating at angles up to $\Theta_0 = 42^\circ$ with respect to the incident beam. Good agreement between calculated and measured peak intensities, up to the sixth order, is obtained by accounting for random deviations in the slit positions, and averaging over the velocity spread of the incident beam as well as the spatial extent of the nozzle beam source. It is demonstrated that He atom beam diffraction together with simple transmission measurements is an excellent means of characterizing such gratings including a detailed determination of the slit width, the bar shape, and random as well as periodic disorder.

PACS number(s): 03.75.Be, 39.20.+q, 81.05.Ys

I. INTRODUCTION

In recent years there has been a very rapid development in using microfabricated structures for the manipulation and analysis of atomic and molecular beams [1]. One of the most interesting of these microfabricated devices is the diffraction grating, which was used first by Keith *et al.* [2] for diffracting an atomic beam of Na atoms. The lighter helium atoms are particularly attractive for such experiments [3,4] since by virtue of their very weak physisorption interactions they do not stick to or contaminate the surface, facilitating the use of delicate structures. Moreover, the beam source can be cooled down to temperatures of several degrees Kelvin leading to much larger diffraction angles than possible with alkali atoms. Recently, our group demonstrated the use of transmission gratings for nondestructively selecting small helium clusters via their different diffraction angles [3,5]. These experiments provided the first unequivocal evidence for the existence of the helium dimer and trimer [3], which by virtue of their very weak binding are difficult to detect by other means. Because of this weak binding, the average radial distance of the dimer is 55 Å [6], making it the largest ground-state diatomic molecule. Recently, the Göttingen group has embarked on a research program to determine the size of the He dimer by a comparative analysis of the He atom and He dimer diffraction intensities [7]. In the course of these studies rather significant discrepancies were found between the measured relative diffraction intensities when compared with calculations based on Kirchhoff's formula [8]. In this theory the relative intensities of the diffracted order peaks are completely determined by the *open fraction*, i.e., the ratio of the width of the slits between the grating bars to the grating period, while the wavelength of the atomic beam, for a given grating period, only determines the angular position of the peaks. Until recently, Kirchhoff's theory, which is very successful in explaining many features of light diffraction, had

been assumed to be valid also for atom diffraction.

At the present time, on the basis of the most recent experiments, it is now believed that a number of effects not incorporated in the Kirchhoff approximation have to be accounted for, including a precise determination of (1) the average slit width, (2) the actual profile of the bars, (3) the statistical randomnesses in the bar edge positions, (4) the long-range attractive C_3/z^3 potential between the projectile and the bars, and (5) the microscopic roughness of the surface of the bars.

In the present paper, high-resolution experimental results on the diffraction of helium atoms from a room-temperature nozzle-beam source, with an incident energy of 65 meV, by a 100 nm-period silicon-nitride grating are used to investigate systematically the first three of the above physical properties of the grating, whereas effects (4) and (5) have been investigated recently [9]. The measured diffraction results are first interpreted with theoretical calculations based on the Kirchhoff diffraction model in the Fresnel approximation, developed for optical gratings. By allowing for a small random distribution of variations in the slit widths and slit positions, and by accounting for the velocity spread and spatial extent of the nozzle beam, both the measured diffraction peak intensities and the background signal between the peaks can be well reproduced. Additional features similar to Lyman ghosts [10–12] become especially apparent when the grating is inclined at large angles with respect to the incident beam, leading to a greater sensitivity to the positions and smoothness of the slit edges [13]. Deviations in peak intensities from the Kirchhoff-based calculations, especially at large angles of inclination, indicate that the interaction potential between the grating and the helium atoms also affects the diffraction pattern [9].

The paper is organized as follows. In Sec. II the experimental apparatus is described, followed by a presentation of the experimental results in Sec. III. Section IV provides a

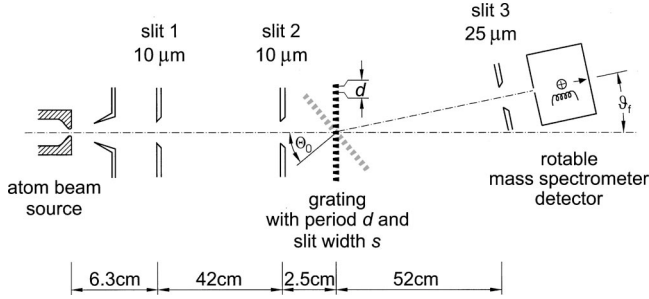


FIG. 1. Schematic top view of the apparatus used in the He atom diffraction experiments. The diffraction grating has a period of 100 nm and can be rotated by an angle Θ_0 about an axis perpendicular to the plane of the page. The gratings are 200 μm wide and 5 mm high.

discussion of the basic diffraction formalisms, grating models and methods for accounting for the incident beam properties and defects in the grating. The experimental results are compared with theoretical calculations in Sec. V and discussed in Sec. VI.

II. EXPERIMENTAL SETUP

A schematic diagram of the experimental setup [3,5] is shown in Fig. 1. The nearly monoenergetic beam of helium atoms is produced by supersonic expansion of pure (99.9999%) helium gas through an electron microscope aperture, which is nominally $5 \pm 1 \mu\text{m}$ in diameter and about 2 μm long. All the present measurements involving helium were made with the source at room temperature $T_0 = 300 \text{ K}$, with a source stagnation pressure of $P_0 = 140 \text{ bar}$, and a source chamber pressure of about $7.5 \times 10^{-4} \text{ mbar}$. Some measurements were also performed with krypton at $T_0 = 300 \text{ K}$ and $P_0 = 50 \text{ bar}$. At these source conditions the fraction of clusters in both atomic beams is expected to be completely negligible [5]. The mean velocity of the helium beam is measured to be $u = 1780 \text{ m/s}$ with a full width at half maximum (FWHM) spread Δv of $\Delta v/u \approx 2.1\%$ and a mean de Broglie wavelength of 0.56 \AA . For efficiently ionizing a tall narrow slit beam the detector utilizes a homemade electron bombardment ionizer, which is followed by a simple low-mass-resolution ($m/\Delta m \approx 40$), magnetic 90° deflection, mass spectrometer. At the electron impact energy of 120 eV the overall efficiency (ions per incident atom) is estimated to be somewhat greater than 10^{-6} , increasing with decreasing atom beam velocity. Four differentially pumped vacuum stages between the grating and detector chamber reduce the total pressure in the latter chamber to less than $1 \times 10^{-11} \text{ mbar}$ corresponding to a background count rate of typically 4 counts/s.

Since the de Broglie wavelength λ of the helium atoms is less than 1 \AA and the grating period d is 1000 \AA , diffraction angles of the order of magnitude of $\lambda/d \approx 1 \text{ mrad}$ are expected. The flight path of the helium beam, as shown in Fig. 1, is parallel to the laboratory floor and the slits are perpendicular to the plane of the floor. Because of the relatively tall slits (5 mm) the effect of gravity can be ne-

glected. In order to achieve the spatial coherence necessary for resolving small diffraction angles, the beam is collimated by two 10- μm -wide 5-mm-tall slits located 63 mm and 482 mm downstream from the source. The transmission grating is placed 25 mm behind the second slit. A third slit, 25 μm wide, is placed in front of the detector entrance 520 mm downstream from the grating. The detector is mounted on a large support which is driven by a stepping motor with an angular displacement of about $0.7 \mu\text{rad}$ per step in a circular path around an axis normal to the laboratory floor and coinciding with the grating slits. The overall effective angular resolution of the apparatus amounts to about $70 \mu\text{rad}$ FWHM as determined from the measured intensity profile of the beam without the grating. Since this is significantly smaller than the estimated angular spacing of the diffraction peaks, they are clearly resolved for the $T_0 = 300 \text{ K}$ helium atom beam.

Because of space limitations, the angular position of the UHV chamber housing the detector ionizer is measured about 20 cm below the beam line. As a result of some torsional bending of the support mount the actual position of the detector ionizer may differ slightly from the indicated angular position. Therefore, in comparing the measured and calculated diffraction patterns (in Fig. 11), the peak positions in the raw data were corrected by rescaling the measured angular positions by a factor 0.84, in order to make them coincide with the angular positions predicted by Kirchhoff's formula.

The transmission diffraction grating is made out of low-stress, nonstoichiometric silicon nitride (SiN_x) using achromatic interferometric lithography and reactive ion etching [14]. As shown in Fig. 2 the grating has overall dimensions of 200 μm width and 5 mm height. The nominal grating period is 100 nm with nominally 50 nm wide bars and slits. As discussed in the next section, the thickness of the grating was determined from measurements of the overall transmission as a function of angle of inclination to be about 90 nm [13]. The arrangement of three gratings on a single chip, their sizes, and the support bars are shown schematically, as well as in the scanning electron micrograph, in Fig. 2. Coarse horizontal support bars 1.5 μm wide with a periodicity of 5 μm perpendicular to the slits maintain the stability of the fine bars. The support bars reduce the overall transmission from 50% to nominally about 30%.

Figure 3 shows a side view of the individual grating bars at an intermediate fabrication step, before the bars have been freed from the silicon substrate, and reveals the truncated wedge shape profile, which was confirmed by the transmission experiments described in the next section. In the experiments described here, the chip is mounted in vacuum on a manipulator which provides for adjusting the three Cartesian coordinates, as well as rotation around an axis perpendicular to the grating plane and rotation around an axis perpendicular to the plane depicted in Fig. 1 enabling measurements under normal and off-normal incidence.

III. EXPERIMENTAL RESULTS

A. Transmission measurements

To characterize the profile of the grating bars, the transmitted intensity was measured as a function of the grating

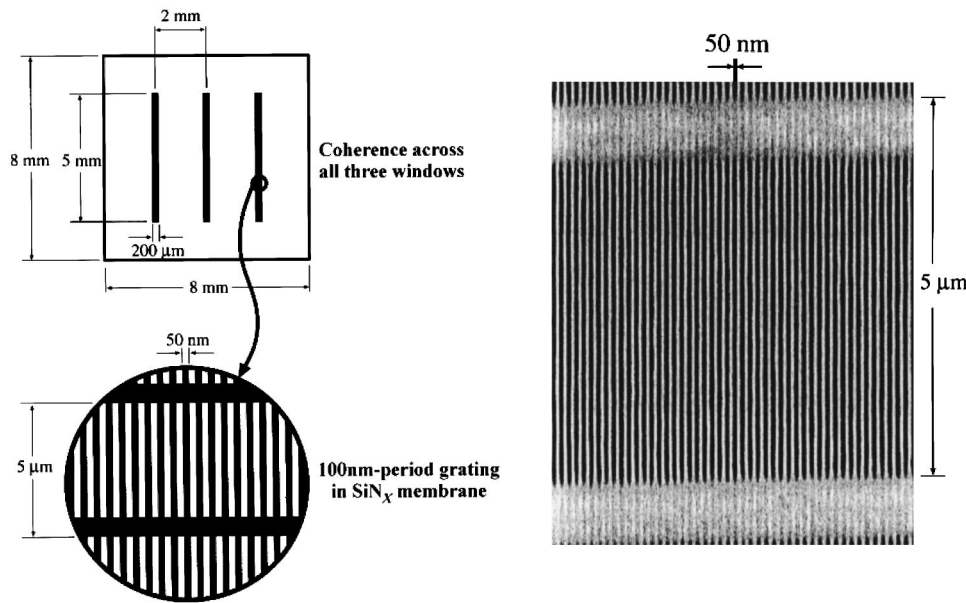


FIG. 2. On the left side, the arrangement of three silicon nitride gratings on a silicon chip is shown. In the experiment only one grating is illuminated by the atomic beam. The right shows an electron micrograph of a small part of a grating. In addition to the fine grating bars, two of the 1- μm -wide support bars, which are spaced 5 μm apart, are clearly seen at the top and bottom of the micrograph.

angle of inclination Θ_0 . In order to collect as many of the diffracted particles, including those diffracted into higher-order peaks, the 25- μm aperture slit in front of the detector was removed (see Fig. 1) to increase the acceptance angle of the detector to about $\Delta\Theta \approx 3.4 \times 10^{-3}$ rad. Figure 4 shows the results of such measurements for He and Kr atom beams. The transmission without inclination of about 30–35% is explained by the expected 50% transmission of the grating, which is further reduced by additional losses due to the horizontal support bars. Despite the increased acceptance angle, helium diffraction orders $n > 3$ did not arrive at the detector and hence went uncoun- ted. Furthermore, at larger angles of inclination, which result in a small decrease of the projected grating period, the diffraction pattern extends to larger total angles and the number of peaks not detected increases to $n > 2$. However, since these higher-order peaks are two to three orders of magnitude smaller in intensity than the cen-

tral peaks, the error caused by this effect is small. Within Kirchhoff's theory in the Fraunhofer limit [Eq. (11) of Sec. IV B] the error is calculated to be 5% for a grating having equally wide slits and bars in the case that orders $n > 3$ are not detected. In the case of krypton, due to its much smaller de Broglie wavelength (0.12 Å), diffraction peaks up to $n = 12$ are still within the acceptance angle of the detector, leading to a slightly larger apparent transmission, as ob-

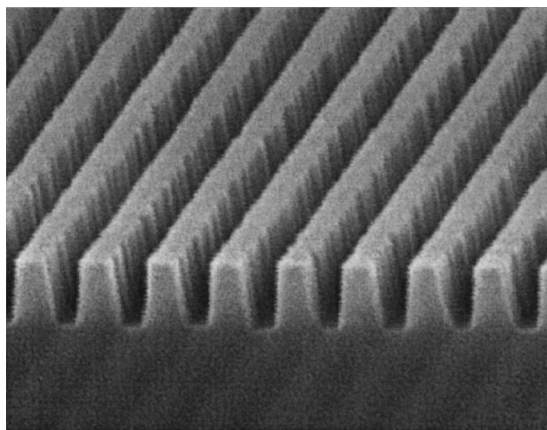


FIG. 3. Electron micrograph of the silicon nitride grating at an intermediate fabrication step before the silicon substrate is removed by reactive ion etching. The truncated wedge shape geometry of the grating bars is clearly visible confirming the interpretation of the transmission shown in Fig. 4.

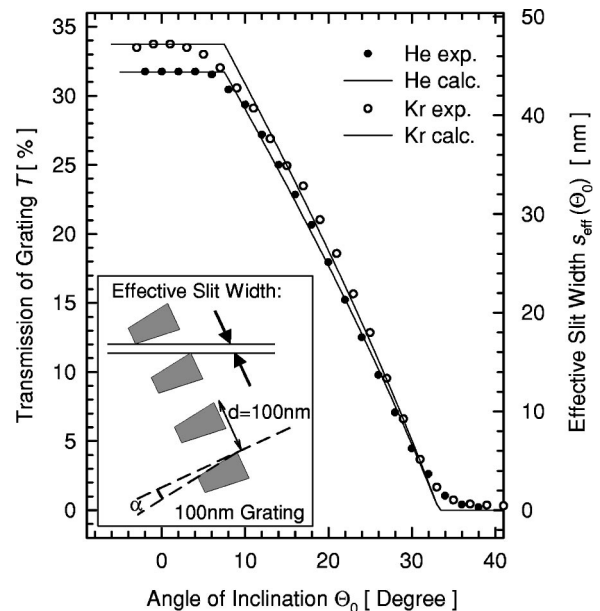


FIG. 4. Measured total transmitted intensity as a function of grating angle of inclination Θ_0 for He (filled circles) and for Kr atom beams (open circles) of energy $E_i = 65$ meV ($T_0 = 300$ K) for grating I. In combination with analysis of diffraction intensities, the transmission can be used to calibrate the effective slit width $s_{\text{eff}}(\Theta_0)$ as plotted on the right vertical axis. The lines are fits assuming a truncated wedge shape cross section of the grating bars as depicted in the inset, revealing a grating thickness of 90 nm and a wedge angle $\alpha = 7.5^\circ$.

served in Fig. 4. For normal incidence the krypton transmission is measured to be 33.7% in comparison to 31.7% for helium, the difference being in very good agreement with the expected 5% additional loss for helium. Otherwise, the observed dependence on the angle of inclination Θ_0 for Kr is nearly identical with that for helium.

As seen in Fig. 4, for the first 7° of inclination the intensity remains almost constant. This is explained by the cross-sectional shape of the grating bars. The results in Fig. 4 are consistent with bars that are narrower at the front than at the back, or bars that are wider at the front than at the back side, and thus up to a certain angle of inclination the effective slit width is not reduced. Beyond $\Theta_0=7^\circ$ the total transmitted intensity decreases nearly linearly with Θ_0 , consistent with a decreasing effective slit width s_{eff} as shown in the inset of Fig. 4 [15]. Up to about $\Theta_0=31^\circ$ the transmission decreases linearly to a value of approximately 3% corresponding to an average effective slit width of 4.2 nm and then tapers off and falls off more slowly. The dependence of the transmission on the angle of inclination is fitted well (continuous line) if truncated wedge shaped cross sections with sharp perfectly straight edges are assumed for the grating bars as shown in the inset of Fig. 4. From the slope of the curve and the extrapolated cutoff angle of about 33° a grating thickness of 90 nm and a wedge angle α equal to 7.5° were determined from the best fit. This wedge angle is in good agreement with the electron microscope view of the grating bars shown in Fig. 3. The small tail in the transmission beyond 31° is attributed to the roughness of the grating bar edges and to the nonuniformity in the positions of the bar edges.

The effective slit width can be simply calculated from the transmitted intensity, $T(\Theta_0)$,

$$s_{\text{eff}}(\Theta_0) = s_{\text{eff}}(\Theta_0=0) \frac{T(\Theta_0)}{T(\Theta_0=0)}. \quad (1)$$

The effective slit width $s_{\text{eff}}(\Theta_0)$ is given on the right-hand vertical axis of Fig. 4. In addition, for off-normal incidence the decrease in the effective grating period $d(\Theta_0)$, and the increase in the number of illuminated slits $N(\Theta_0)$, which depend on the angle of inclination, are given, respectively, by

$$d(\Theta_0) = d(0) \cos \Theta_0, \quad (2)$$

and

$$N(\Theta_0) = \frac{N(0)}{\cos \Theta_0}. \quad (3)$$

For example, for 40° off-normal incidence the period is decreased by 23% and the number of illuminated slits increases from 100 to 131.

B. Diffraction measurements

Figure 5 shows a series of measured diffraction patterns, in which the signal is plotted on a logarithmic scale as a function of the deflection angle ϑ_f for a number of different angles of inclination Θ_0 at an incident beam energy of E_i

$=65$ meV ($T_0=300$ K). For $\Theta_0=0^\circ$ the odd-order peaks are at least an order of magnitude greater than the even-order peaks. This trend is expected from Kirchoff's optical theory in the Fraunhofer limit, according to which the intensities of the diffraction peaks are determined by the slit function envelope [8]. The slit function is simply the diffraction pattern of a single grating slit, as will be discussed in detail in Sec. IV. For a grating with exactly equal slit and bar widths the even-order peaks coincide with the zeros of the envelope slit function and hence should, in fact, be completely suppressed. Thus, the smaller even-order intensities are a sensitive and direct indication that for the present grating the slit and bar widths are not exactly equal. The range of observed intensities is quite large, the most intense peak at zeroth order has an intensity of about 10^5 counts/s, while the smallest peaks observed at normal incidence are the ninth-order which have intensities of approximately 50 counts/s on a background of about 20 counts/s. The ninth-order peaks seen in Fig. 5 are by no means at the limit. For example, in other measurements it has been possible to observe diffraction peaks out to the 23rd order [16].

As the grating angle of inclination is increased, the even-order peaks become more intense, which is expected for the spreading of the slit function which becomes broader as the effective slit width decreases. With increasing angle of inclination up to $\Theta_0 \leq 30^\circ$ the diffraction pattern nicely resembles the expected Fraunhofer pattern. For $\Theta_0 > 30^\circ$ the envelope of the peak intensities deviates increasingly from the behavior expected for the slit function which should become broader and broader with increasing angle of inclination and finally should approach a horizontal line in the limit of vanishing effective slit width. Instead, a much faster decrease of the diffraction intensities with increasing diffraction order is observed, falling off exponentially or even faster for angles of inclination $\Theta_0 > 35^\circ$. As a result, for these angles of inclination the number of observed diffraction peaks begins to decrease significantly, while the maximum intensity has dropped to slightly more than 100 counts/s. At the largest angle of inclination, $\Theta_0=42^\circ$, the maximum intensity is less than 100 counts/s but still peaks out to the $n=3$ order can be clearly seen.

These deviations from the predictions of optical theory for a perfect grating are attributed mainly to two opposing effects. The first one, due to the van der Waals interaction between the helium atoms and the silicon nitride of the grating bars, introduces an additional narrowing of the effective slit width [9], which depends on the geometry of the slits and bars and is expected to be increasingly important at large angles of inclination where the effective slit width is smallest. The second effect, resulting from the roughness in the slit edges and fluctuations in the slit edge positions and their spacings, leads to an increase in the intensity falloff with increasing diffraction order and thus appears to be the dominant effect. It will be analyzed quantitatively in Sec. V A.

At angles of inclination $\Theta_0 \geq 27^\circ$ very small additional peaks can be seen as satellites at angles at about $2/3$ of the angle of the first-order peaks. With increasing Θ_0 additional small peaks appear at about $1/3$ of the first order peak angle and begin to appear between the higher order peaks and be-

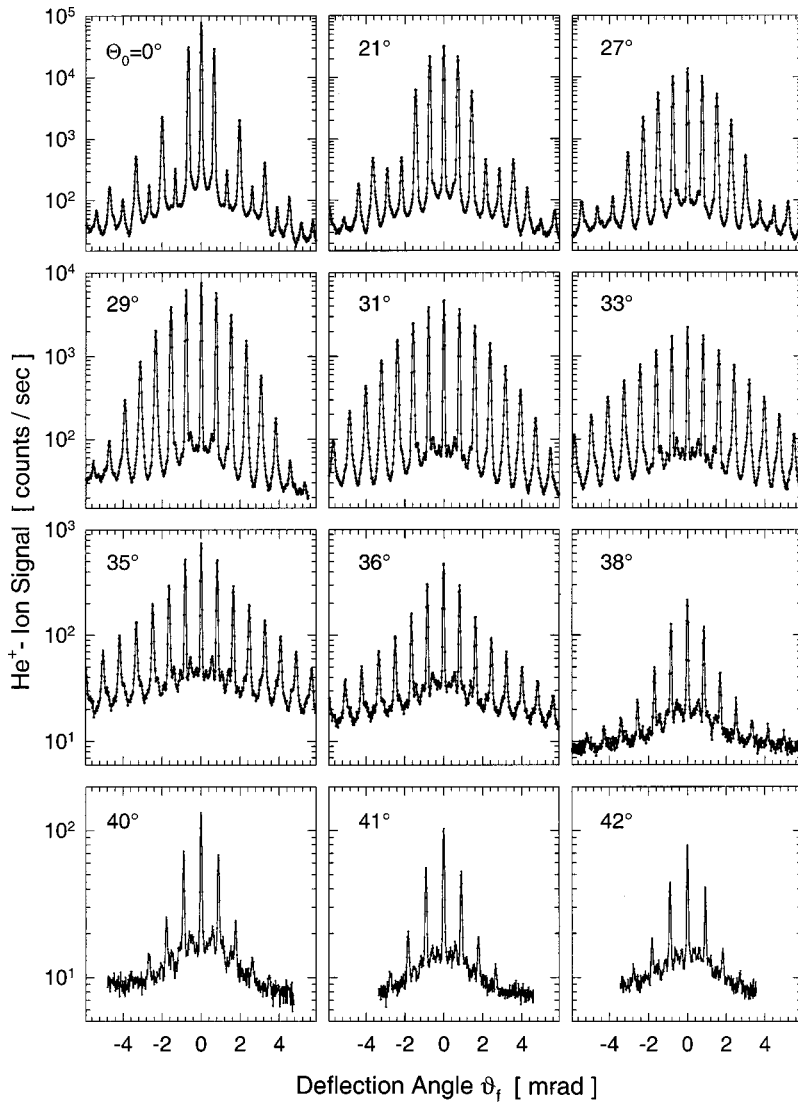


FIG. 5. Experimentally observed diffraction intensities for a He beam of incident energy $E_i = 65$ meV for several different angles of inclination up to $\Theta_0 = 42^\circ$ plotted as a function of deflection angle ϑ_f for grating I. The stagnation temperature and pressure in the source chamber were $T_0 = 300$ K and $P_0 = 140$ bar, respectively, and the measured speed ratio was 77.

come increasingly evident for increasing angles of inclination. These structures cannot be explained by the diffraction of small helium clusters [3,5] since peaks due to clusters are largest near the central peak and, moreover, are expected to decrease with the overall transmitted intensity and would therefore disappear with increasing angle of inclination.

These additional peaks are similar to a phenomenon designated Lyman ghosts [10,12,17], which was observed in the early days of mechanically ruled optical interference gratings. They are caused by small superimposed periodic fluctuations in the grating period which are hard to detect by any other means. Periodic defects are not expected to occur in holographically produced gratings, as used in these experiments, since these rely on the wavelength of light which is fixed by the laser used and is uniform over the surface of the grating. Periodic imperfections could, however, be introduced in the subsequent series of processes which are involved in the grating fabrication [14] as discussed in the Appendix. In the present case, the observed angular positions of the ghost peaks, tentatively attributed to Lyman ghosts, correspond to a period slightly larger than three grating periods.

Moreover, it should be emphasized that the evidence for the ghost peaks is not as direct at $\Theta_0 = 0^\circ$ and is implied only by the very low intensity (10^{-3} of the central peak) shoulders on the side of the first-order peak and some of the higher-order peaks, such as the seventh-order peak (see Fig. 5). It is important to note that the ghost peaks increase strongly in relative intensity with increasing angle of inclination and increase to about 5% of the central peak at large angles of inclination. This suggests that periodic fluctuations in the grating thickness and not so much in the widths are the major contributing factor. Of course, both affect the positions of the bar edges which determine the effective openings. Periodic oscillations in the thickness of the grating can easily occur in the course of the chemical etching (see Appendix).

There is also the possibility that there are additional periodic fluctuations in the grating period extending over a larger number of periods, which would give rise to Rowland ghosts [11,17]. However, Rowland ghosts are expected to give rise to supplementary peaks very close to the main diffraction peaks, where they are more difficult to resolve. No clear evidence for Rowland ghosts could be found.

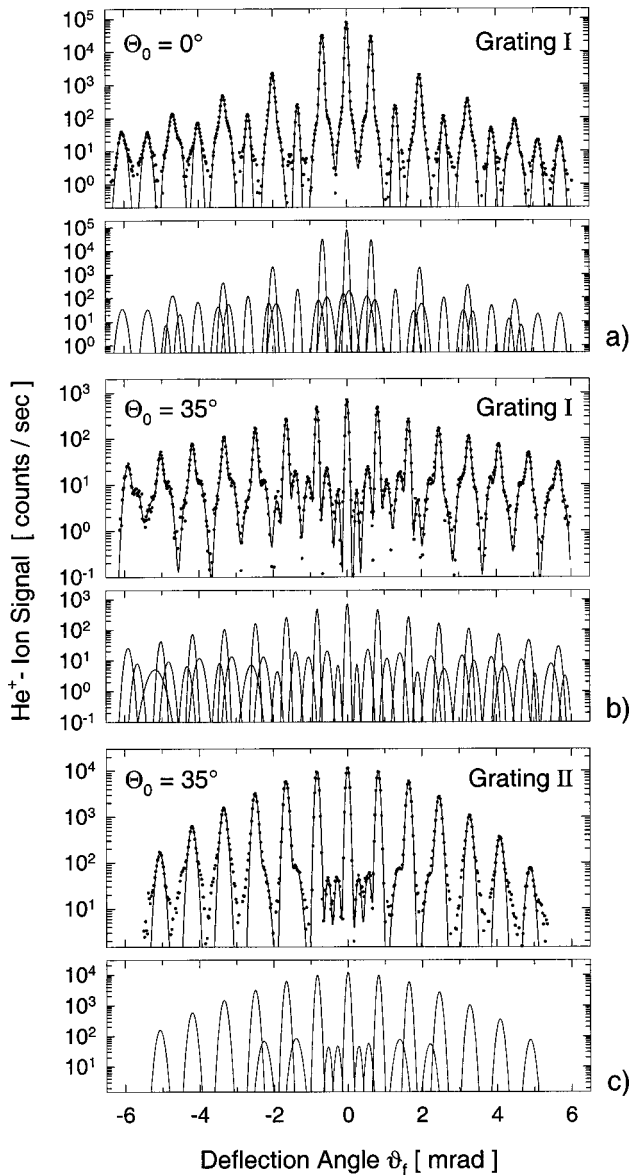


FIG. 6. Examples of the diffraction spectra from grating I fitted by a sum of Gaussians for $\Theta_0 = 0^\circ$ (a), 35° (b), and for grating II at $\Theta_0 = 35^\circ$ (c). Shown in the upper part of each graph is the final fit. Shown below are the individual Gaussian peaks which make up the final fit. The small Gaussians on either side of the main peaks fit the ghost peaks discussed in the text.

In order to extract the positions of the ghost peaks as well as the main diffraction peak intensities, an analysis of each of the diffraction spectra was made by fitting to a sum of assumed Gaussian diffraction peaks. This analysis was carried out for all measured values of Θ_0 , and three examples for such an analysis carried out for two different gratings are shown in Fig. 6. In each case, prior to the fitting procedure, the background intensity was subtracted from the measured data by a linear interpolation between the minima between neighboring peaks. A comparison of the resulting data with best fits is shown in Fig. 6(a) for normal incidence and for $\Theta_0 = 35^\circ$, for two different gratings in Figs. 6(b) and 6(c). It was necessary to include small Gaussian peaks near to and

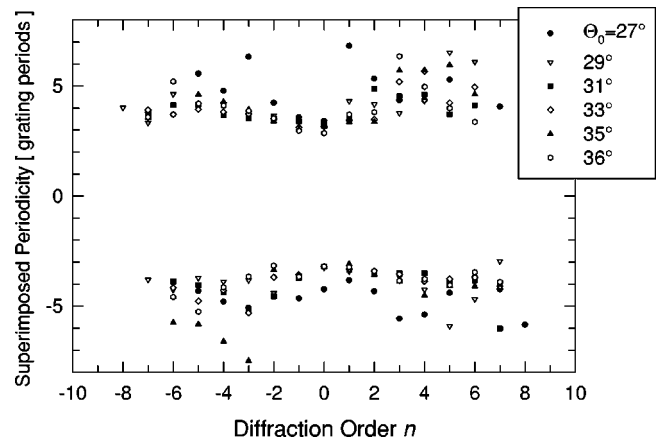


FIG. 7. The angle between neighboring main diffraction peaks divided by the angle between the main diffraction peak and its nearest ghost peak, plotted against the diffraction order. The data points are approximately centered around the value 3.5 indicating a superperiodicity of $3.5d$ or 350 nm.

on either side of the diffraction peaks in order to fit the shoulders or distinct ghost peaks which are the small features tentatively attributed to the Lyman peaks. These, in accordance with standard theoretical interpretations [12], are assumed to be associated with the nearest main diffraction peak. Figure 7 shows the angular positions of the ghost peaks relative to the angle of the neighboring main diffraction peaks for six of the larger values of Θ_0 as a function of diffraction order. This fractional angle is approximately 3.5, which implies that the supposed Lyman peaks are due to a superimposed periodicity of about $3.5d = 350$ nm.

It would, in principle, be possible to model the ghost peaks and hence to analyze also their intensities. But there are too many ways to model these peaks, because the superperiodicity could be caused by a number of different mechanisms: a superperiodicity in the grating period, in the size of the bars or slits, in the shape of the bars or slits, in the grating thickness as mentioned above, or in many other aspects of the grating. Since the currently available experimental data is not sufficient to distinguish which would be correct, a modeling of the ghost peaks has not been carried out.

The results shown in Fig. 6(c) for $\Theta_0 = 35^\circ$ were obtained with a newer 100 nm-period grating (grating II). Since it has a larger slit width of almost 60 nm and the measurement was done with somewhat broader collimating slits, the peak widths are increased and peak intensities are more than an order of magnitude larger. Furthermore, the peak envelope resembles more the slit function expected from optical theory as compared to Fig. 6(b). This can be interpreted as a result of the larger effective slit width, which decreases the effect of the van der Waals interaction between the helium atoms and the grating bars, thereby reducing the relative deviations from the optical behavior. In addition, the small ghost peaks are apparently much less pronounced, demonstrating the greater uniformity in the structure of this grating, which was produced after the results shown in Fig. 6(b) indicated the need for further optimization of the fabrication process.

IV. THEORY

A. Basic formulas

The calculation of the diffraction pattern produced by a transmitting object like a grating is a standard problem in optics. If the atomic particle is infinitesimally small and is assumed not to interact with a grating bar unless it strikes it directly, then optical theory is expected to be applicable. In this case the atom beam can be described by a spherical wave, which is generated from a point source $\mathbf{R}_0 = (x_0, y_0, -z_0)$, with $R_0 = \sqrt{x_0^2 + y_0^2 + z_0^2}$ where $x_0, y_0,$ and $z_0 > 0$ are measured with respect to the transmitting object at $x = y = z = 0$. The diffraction problem is described completely by the solution of the wave equation for propagation in the z direction through an opening in the object placed at $z = 0$ once the appropriate boundary conditions have been specified. The amplitude $\psi(\mathbf{R})$ of the diffracted wave at an observation point $\mathbf{R} = (x, y, z)$ with $R = \sqrt{x^2 + y^2 + z^2}$ is then given by the Helmholtz-Kirchhoff integral theorem [8]. For simplicity a one-dimensional aperture is assumed, which also implies taking $y = y_0 = 0$, so that the intensity distribution $\mathcal{I} = |\psi(\mathbf{R})|^2$ is a function only of the incident and scattered polar angles ϑ'_i and ϑ'_f which are defined by the relations $x_0 = -R_0 \sin \vartheta'_i$, $z_0 = R_0 \cos \vartheta'_i$, $x = R \sin \vartheta'_f$, and $z = R \cos \vartheta'_f$ as depicted in Fig. 8. If the characteristic dimension of the aperture is small compared to R and R_0 , then the intensity is given by the Fresnel limit of the Helmholtz-Kirchhoff integral [8]

$$\begin{aligned} \mathcal{I}(\vartheta'_i, \vartheta'_f) &= |\mathcal{A}(\vartheta'_i, \vartheta'_f)|^2 \\ &= \mathcal{I}_0 k^2 \left| \int_{-\infty}^{\infty} dx \exp \left[i \frac{k}{2} \left(\frac{\cos^2 \vartheta'_f}{R} + \frac{\cos^2 \vartheta'_i}{R_0} \right) x^2 \right] \right. \\ &\quad \left. \times \exp[-ik(\sin \vartheta'_f - \sin \vartheta'_i)x] t(x) \right|^2, \end{aligned} \quad (4)$$

where $k = 2\pi/\lambda$ and λ is the de Broglie wavelength. In Eq. (4), $t(x)$ is the transmission function of the aperture which in general is a complex function

$$t(x) = t_0(x) e^{i\varphi(x)}. \quad (5)$$

In the simplest case of the usual Kirchhoff extinction boundary conditions, $t(x) = 0$ at the position of the grating bars and $t(x) = 1$ in the slits between the bars. Equation (4) represents the diffraction intensity for a geometry in which the grating lies in the plane $z = 0$.

When the grating is inclined by an angle Θ_0 the actual experimental deflection angle ϑ_f is no longer of the same order of ϑ'_f , since under the present experimental conditions $\Theta_0 \gg \vartheta_f$ (see Fig. 8). Thus, in order to make direct comparisons with the measured diffraction spectra for $\Theta_0 \neq 0$ it is convenient to set $\vartheta'_f = \Theta_0 + \vartheta_f$. The same reasoning can be made with the incident angle ϑ'_i which becomes $\vartheta'_i = \Theta_0 + \vartheta_i$. Substituting these expressions in Eq. (4) and making an expansion consistent with small ϑ_i and ϑ_f leads to

$$\begin{aligned} \mathcal{I}(\vartheta_i, \vartheta_f) &= \mathcal{I}_0 k^2 \left| \int_{-\infty}^{\infty} dx \exp \left[i \frac{k}{2} \cos^2 \Theta_0 \left(\frac{1}{R} + \frac{1}{R_0} \right) x^2 \right] \right. \\ &\quad \left. \times \exp[-ik \cos \Theta_0 (\sin \vartheta_f - \sin \vartheta_i)x] \right. \\ &\quad \left. \times \exp[-ik \sin \Theta_0 (\cos \vartheta_f - \cos \vartheta_i)x] t(x) \right|^2, \end{aligned} \quad (6)$$

where terms of the order $x^2 \sin^2 \vartheta_i / R$ have been neglected. Equation (6) has been used in Sec. VB to simulate diffraction patterns at different angles of inclination Θ_0 in the Fresnel limit.

A further simplification is possible if the maximum dimension of the aperture x_{max} is such that

$$\frac{\pi(x_{max})^2}{\lambda} \left(\frac{1}{R} + \frac{1}{R_0} \right) \ll 1. \quad (7)$$

In this case Eq. (4) reduces to the Fraunhofer diffraction formula in which the intensity distribution is given simply by the Fourier transform of the transmission function $t(x)$

$$\mathcal{I}(\kappa) = |\mathcal{A}(\kappa)|^2 = \mathcal{I}_0 k^2 \left| \int_{-\infty}^{\infty} dx e^{-i\kappa x} t(x) \right|^2, \quad (8)$$

where $\kappa = k(\sin \vartheta_f - \sin \vartheta_i)$.

B. Grating models

Within the above theory, a diffraction grating is completely described in terms of the transmission function $t(x)$. Once an appropriate model for $t(x)$ has been chosen, the diffracted intensity distribution is determined via Eq. (4) or Eq. (8). In the present discussion it is assumed that the atoms interact with the diffraction bars via a hard wall potential thereby altering only the amplitude and not the phase of the incident wave field. In this special case $\varphi = 0$ in Eq. (5) and one speaks of an *amplitude grating*. For an amplitude grating, $t(x)$ can be expressed as the sum of the transmission functions of each periodic element

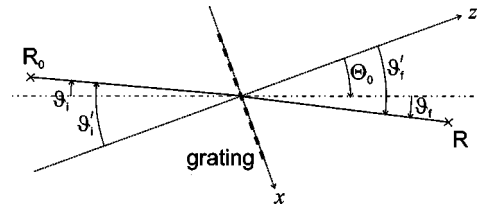


FIG. 8. Definition of the coordinate system. The x axis lies in the grating plane, perpendicular to the grating slits, the z axis is defined parallel to the grating normal, while the y axis is perpendicular to the paper plane. The angles ϑ_i and ϑ_f as well as the angle of inclination Θ_0 are defined with respect to the apparatus axis (dash-dotted line) defined in Fig. 1. \mathbf{R} and \mathbf{R}_0 are vectors defined in Sec. IV A.

$$t(x) = t_0(x) = \sum_{j=1}^N t_{0j}(x), \quad (9)$$

with N the number of illuminated slits. For a grating consisting of a succession of equidistant slits, each of width s , Kirchhoff's extinction boundary conditions imply the following form for $t_{0j}(x)$:

$$t_{0j}(x) = \begin{cases} 1, & \left(\frac{N+1}{2} - j\right)d - \frac{s}{2} \leq x \leq \left(\frac{N+1}{2} - j\right)d + \frac{s}{2}, \\ 0, & \text{otherwise,} \end{cases} \quad (10)$$

where d is the grating period. In the Fraunhofer limit, the substitution of Eq. (10) in Eq. (8) yields the well-known formula

$$\mathcal{I}(\kappa) = \mathcal{I}_0 k s^2 \left[\frac{\sin\left(\frac{1}{2}\kappa s\right)}{\frac{1}{2}\kappa s} \right]^2 \left[\frac{\sin\left(\frac{N}{2}\kappa d\right)}{\sin\left(\frac{1}{2}\kappa d\right)} \right]^2, \quad (11)$$

where the first factor in brackets is the sinc function. Since it depends only on the slit width s it is called the *slit function*. The second factor which involves the ratio of two sine functions, is called the *grating function* since it depends only on the grating period d . The position of the main order peak intensities is determined by $\kappa = n(2\pi/d)$, $n = 0, \pm 1, \pm 2, \dots$. For small diffraction angles and zero incidence angle the angular positions can be approximated by

$$\vartheta_f^{(n)} \simeq n \frac{\lambda}{d}. \quad (12)$$

When the grating is inclined by an angle Θ_0 the angular positions of the main diffraction peaks are scaled to larger values as compared to Eq. (12) according to

$$\vartheta_f^{(n)} \simeq n \frac{\lambda}{d \cos \Theta_0}, \quad (13)$$

which is a good approximation since $\vartheta_f^{(n)} \ll \Theta_0$ holds even for the highest orders observed in this work ($n = 10$).

C. Grating defects

Equation (11) is for an idealized, perfectly ordered diffraction grating. Real gratings are subject to a number of defects which can significantly affect the intensities of the diffraction pattern, and as discussed in the previous section can even give rise to spurious peaks in the intensity which can be mistakenly attributed to other phenomena. Possible defects include (1) *periodic* errors in the spacing and widths of the bars and (2) *random* errors in the period, spacing, and widths of the grating bars. Periodic errors give rise to the already mentioned Lyman ghosts [10] and Rowland ghosts [11]. The most straightforward way to account for either periodic or random errors is through the transmission function. The errors can be described by introducing the displacements of the center of the j th slit about its periodic position denoted by δd_j and also the displacements of the leading edge of the slit denoted by δs_{1j} and displacements of the trailing edge of the slit given by δs_{2j} . Then the transmission function becomes

$$t_{0j}(x) = \begin{cases} 1, & \left(\frac{N+1}{2} - j\right)d + \delta d_j - \left(\frac{s}{2} + \delta s_{1j}\right) \leq x \leq \left(\frac{N+1}{2} - j\right)d + \delta d_j + \left(\frac{s}{2} + \delta s_{2j}\right), \\ 0, & \text{otherwise.} \end{cases} \quad (14)$$

The final intensity distribution will then be the average of $\mathcal{I}(\vartheta_i, \vartheta_f)$ over all the distribution probabilities of the various displacements $\delta d_1, \delta s_{11}, \delta s_{21}, \dots, \delta d_N, \delta s_{1N}, \delta s_{2N}$, that is

$$\bar{\mathcal{I}}(\vartheta_i, \vartheta_f) = \int_{-\infty}^{\infty} d\delta d_1 \cdots \int_{-\infty}^{\infty} d\delta s_{2N} f_d(\delta d_1) \cdots f_s(\delta s_{2N}) \mathcal{I}(\vartheta_i, \vartheta_f), \quad (15)$$

where the $f_s(\delta s)$ and $f_d(\delta d)$ are distribution functions. An example of the latter are random variations given by independent Gaussian distributions:

$$f_d(\delta d) = \frac{1}{\sqrt{2\pi}\sigma_d} \exp\left[-\frac{(\delta d)^2}{2\sigma_d^2}\right], \quad (16)$$

$$f_s(\delta s) = \frac{1}{\sqrt{2\pi}\sigma_s} \exp\left[-\frac{(\delta s)^2}{2\sigma_s^2}\right], \quad (17)$$

where σ_d and σ_s represent the mean square displacements of the slit positions and edges, i.e., $\sigma_d^2 = \langle \delta d^2 \rangle$ and $\sigma_s^2 = \langle \delta s^2 \rangle$. Since Eqs. (15)–(17) are well suited to numerical evaluation, they have been used in Sec. V B to simulate random disorder in the gratings.

D. Analogy to Debye-Waller attenuation

The inclusion of random variations of the slits and periodicity of the grating, such as given by the Gaussian distributions, Eqs. (16) and (17), changes the overall intensity of the diffraction pattern, and in particular the intensities of the

main maxima are reduced. An analytical result is obtained in the Fraunhofer limit if the scattering amplitude $\mathcal{A}(\kappa)$ of Eq. (8) is calculated using the transmission function of Eq. (14). After averaging over the Gaussian distribution functions, Eqs. (16) and (17), the final result is

$$\begin{aligned} \bar{\mathcal{A}}(\kappa) &= \int_{-\infty}^{\infty} d\delta d_1 \cdots \int_{-\infty}^{\infty} d\delta s_{2N} f_d(\delta d_1) \cdots f_s(\delta s_{2N}) \mathcal{A}(\kappa) \\ &\propto \left\{ \frac{\sin\left[\frac{1}{2}\kappa s - \frac{1}{4}\kappa^2(\sigma_{s_1}^2 - \sigma_{s_2}^2)\right]}{\frac{1}{2}\kappa s} \right\} \\ &\quad \times \left[\frac{\sin\left(\frac{N}{2}\kappa d\right)}{\sin\left(\frac{1}{2}\kappa d\right)} \right] \exp(-\kappa^2\sigma_d^2/2) \\ &\quad \times \exp[-\kappa^2(\sigma_{s_1}^2 + \sigma_{s_2}^2)/4]. \end{aligned} \quad (18)$$

The diffraction intensity $|\bar{\mathcal{A}}(\kappa)|^2$, that has been applied to analyze the data in Sec. V A, is similar to the simple Fraunhofer result, Eq. (11), except for two important differences. First, the additional term $-\kappa^2(\sigma_{s_1}^2 - \sigma_{s_2}^2)/4$ in the slit function in the curly brackets can introduce an asymmetry in the overall diffraction pattern if the mean square displacements of the leading and trailing edges of the slit are unequal. Second, the overall intensity of the diffraction pattern, and in particular the intensities of the maxima, are reduced by the last two exponential factors in Eq. (18). This apparent loss of total intensity can be readily explained by the more general averaging process applied directly to the intensity rather than to the amplitude. A simple calculation shows that the reduction in intensity of the diffraction maxima is identical to that in Eq. (18). Moreover, there is a compensating increase of the diffuse background in analogy with the scattering by thermally induced roughness for two-dimensional surfaces [18].

This analysis shows that random disorder in the grating spacing has the effect of reducing all diffraction peaks with the concomitant increase of a broad background of incoherent diffuse scattering. As a particular example, for the special case of a grating with bars and slits, which on average are equally wide, the even-order diffraction peaks will still have zero intensity and the effect of random disorder of the sort described by Eqs. (16) or (17) will not cause small intensity peaks at the even-order positions. Thus, the small even-order peaks apparent in the experimental data of Fig. 5 for normal incidence indicate that the average bar width to slit width ratio differs slightly from unity.

Finally, it should be mentioned that the averaging analysis of Eqs. (15)–(17) which leads to the result of Eq. (18) can also be analytically applied to the full Fresnel limit intensity of Eq. (4). The result is that Eq. (18) becomes multiplied by correction terms, all of which go to unity in the limit of R and R_0 becoming large compared to the grating period.

The two Gaussian-like exponential factors appearing in

Eq. (18), which depend both on the momentum transfer and the mean square displacements, are analogous to the Debye-Waller factors which arise in the theory of scattering of fast projectiles from vibrating targets [19]. In both cases the dependence on the scattering wave vector κ is identical. In the present case the mean square displacement is due to static random displacements in the grating positions whereas in the case of the Debye-Waller factor the displacements are due to dynamical vibrational motions of the atoms of the scattering target.

In order to estimate the importance of the Gaussian factors, in Eq. (18) it is useful to note that for the present gratings ($d=100$ nm) the main diffraction orders are given by $\kappa^{(n)}=n2\pi/d=n\times 0.063$ nm⁻¹. Thus, the arguments $\kappa\sigma$ of the two Gaussian factors increase linearly with both n and σ but do not depend upon the de Broglie wavelength. If the total mean square displacement of the slit edge positions is 10% of the slit width, or 5 nm, then $(\kappa\sigma)^2$ varies from about 0.1 for $n=1$ to 10 for $n=10$. This leads to a significant damping of the diffraction intensities, reducing the first-order peak to 90% and the tenth order even down to 5×10^{-5} of its value for an ideal grating. This effect can largely explain the observed sharp decrease in the diffraction intensities with increasing Θ_0 evident in Fig. 5. Instead of remaining nearly constant with higher order as expected for the slit function of a narrow slit they are observed to fall off rapidly. Moreover, Eq. (18) implies that the observation of high-order diffraction intensities depends crucially on the uniformity of the grating structure.

E. Incoherence due to the finite size and velocity spread of the jet beam source

Equations (4) and (15) describe the diffraction intensity distribution due to a monochromatic spherical wave from a single point source. In order to make comparisons with experimental diffraction peak intensities, the real geometry of the apparatus and the incoherence of the atomic beam source due to its velocity distribution and its spatial extent also have to be accounted for.

In a simple approximation, the supersonic expansion beyond the nozzle is divided by a *freezing zone* into two regimes, the continuum hydrodynamic flow region inside the sudden freeze radius R_{sf} , followed by a free-molecular, collisionless region [20,21] outside this sphere. By treating the expansion as spherically symmetric, the flow in the hydrodynamic region is directed radially outward from the jet orifice to the sudden freeze radius. Beyond the sudden freeze radius no further collisions are assumed to occur between particles. Thus, each point on the sudden freeze radius acts as an independent effective point source for which Eq. (4) or (15) can be applied. Consequently, the observed intensity will be the weighted incoherent summation of Eq. (4) or (8) over the spatial distribution of the sudden freeze surface and the distribution over velocities of the atoms emitted from this surface.

The important geometrical features of the present apparatus are shown schematically in Fig. 9. The lateral dimensions of the source, the sudden freeze radius and the two collimating slits a_1 and a_2 in front of the grating are greatly exagger-

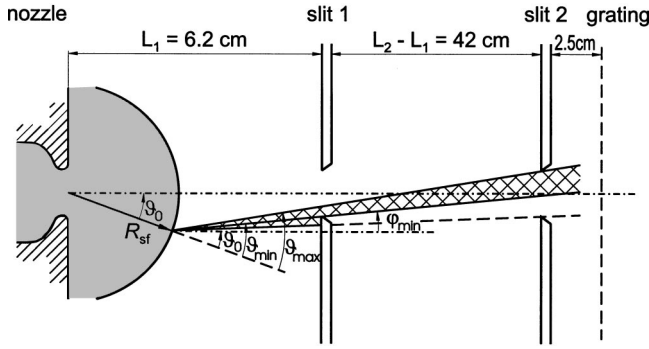


FIG. 9. Schematic top view of the atomic trajectories in the apparatus. The shaded area near the nozzle indicates the hydrodynamic continuum which ends at the sudden freeze zone at a distance R_{sf} from the center of the nozzle orifice. From a point on the sudden freeze area the atoms are emitted with an angular and velocity distribution characterized by the speed ratio S . Only atoms which can pass through the collimating slits arrive at and are diffracted by the grating.

ated compared to the z direction. The two slits serve to collimate the beam and to increase the spatial coherence of the source by reducing the area of the sudden freeze surface which contributes to the incident flux illuminating the grating. This reduced area can be expressed geometrically as contained within the small polar angle ϑ_0^{max} (see Fig. 9) about the z axis on the sudden freeze sphere which, by assuming $a_1 = a_2 \equiv a$, is given by

$$\sin \vartheta_0^{max} = \frac{a}{2R_{sf}} \left[1 + 2 \frac{L_1}{L_2} \left(1 - \frac{R_{sf} \cos \vartheta_0^{max}}{L_1} \right) \right]. \quad (19)$$

In the present case the sudden freeze radius is approximately $R_{sf} \lesssim 1$ mm, the collimating slits 1 and 2 are $10 \mu\text{m}$ wide and the distances L_1 and L_2 are large in comparison. Thus Eq. (19) can be simplified to give

$$\vartheta_0^{max} \approx \frac{a}{2R_{sf}} \left(1 + 2 \frac{L_1}{L_2} \right). \quad (20)$$

The sudden freeze radius can be calculated from the source aperture diameter d_0 and the measured speed ratio S (see below) [22]

$$R_{sf} = 0.2S^{3/2}d_0. \quad (21)$$

The next task is to develop a distribution function for the angular and velocity distribution of particles emanating from each point on the sudden freeze surface. A simple but accurate velocity distribution model is the so-called ellipsoidal Maxwellian model, which assumes two Gaussian distributions with different widths [23]

$$f_{\text{ell}}(v_{\parallel}, v_{\perp}) = \mathcal{N}(v_{\parallel}^2 + v_{\perp}^2) \exp \left[-\frac{m}{2k_B T_{\parallel}} (v_{\parallel} - u)^2 \right] \times \exp \left[-\frac{m}{2k_B T_{\perp}} v_{\perp}^2 \right], \quad (22)$$

where k_B is the Boltzmann constant, \mathcal{N} is a normalization factor, the two parameters T_{\parallel} and T_{\perp} are the parallel and perpendicular temperatures, and, similarly, v_{\parallel} and v_{\perp} are the velocities parallel and perpendicular to the direction of the beam with a most probable velocity u . Up to the freezing radius $T_{\perp} = T_{\parallel}$. Beyond the freezing radius T_{\parallel} remains constant at larger distance from the orifice, while T_{\perp} continues to fall off approximately like $T_{\perp} \sim (z/d_0)^{-2}$ due to geometrical effects, where z is the distance from the orifice [23]. Defining the angle $\vartheta = \vartheta_0 + \vartheta_i$, where ϑ_i is as before the angle of incidence, the velocity v is given by $v^2 = v_{\parallel}^2 + v_{\perp}^2$ with components $v_{\parallel} = v \cos \vartheta$ and $v_{\perp} = v \sin \vartheta$. By making use of small-angle approximations for ϑ , Eq. (22) becomes

$$f_{\text{ell}}(v_{\parallel}, v_{\perp}) = f_{\text{ell}}(v, \vartheta) = \mathcal{N}v^2 \exp \left[-\left(\frac{v-u}{u} \right)^2 S^2 \right] \exp \left(-\vartheta^2 S^2 \frac{v}{u} \right), \quad (23)$$

where

$$S^2 = \frac{\frac{1}{2}mu^2}{k_B T_{\parallel}}. \quad (24)$$

For very narrow velocity distributions $v \approx u$, and the term v/u can be set equal to unity in the second exponential function. In this limit the function $f(v) = c_f v^2 \exp\{-[(v-u)/u]^2 S^2\}$ describes the velocity distribution and the function $\exp\{-\vartheta^2 S^2\}$, the angular distribution, where the two parameters u and S are determined experimentally, and c_f is a normalization constant. The speed ratio S is related to the experimental velocity distribution via

$$S = 2\sqrt{\ln 2} \frac{u}{\Delta v} \approx 1.67 \frac{u}{\Delta v}, \quad (25)$$

where Δv is the FWHM of the velocity distribution. With these assumptions, the observed intensity distribution I_{obs} is given by the weighted average of the intensity

$$I_{obs}(\vartheta_f) = \int_0^{\infty} dv f(v) \int_{-\vartheta_0^{max}}^{\vartheta_0^{max}} d\vartheta_0 \int_{-\pi/2}^{\pi/2} d\vartheta g(\vartheta, \vartheta_0) \mathcal{I}(\vartheta_i, \vartheta_f), \quad (26)$$

with $\mathcal{I}(\vartheta_i, \vartheta_f)$ given by either Eq. (6) or Eq. (8) in the Fresnel or Fraunhofer case, respectively. Equation (26) in the Fresnel case has been used in Sec. VB to simulate the diffraction measurements. The angular distribution is completely specified by

$$g(\vartheta, \vartheta_0) = c_g \chi(\vartheta, \vartheta_0) e^{-\vartheta^2 S^2}, \quad (27)$$

where the factor c_g is a normalization constant. The function $\chi(\vartheta, \vartheta_0)$ takes into account that the classically allowed paths

with initial values of ϑ are confined by ϑ_0 and the dimensions of the two collimating slits, as can be seen in Fig. 9, i.e.,

$$\chi(\vartheta, \vartheta_0) = \begin{cases} 1, & \vartheta_{\min}(\vartheta_0) \leq \vartheta \leq \vartheta_{\max}(\vartheta_0), \\ 0, & \text{otherwise,} \end{cases} \quad (28)$$

where the angles $\vartheta_{\min}(\vartheta_0)$ and $\vartheta_{\max}(\vartheta_0)$ can be approximated as

$$\vartheta_{\min}(\vartheta_0) \approx \begin{cases} -\vartheta_0 - \left[\frac{R_{\text{sf}}}{L_1} (\vartheta_0 + \vartheta^*) \right], & \vartheta_0 \leq -\vartheta^*, \\ -\vartheta_0 - \left[\frac{R_{\text{sf}}}{L_1 + L_2} (\vartheta_0 + \vartheta^*) \right], & \vartheta_0 > -\vartheta^*, \end{cases} \quad (29)$$

$$\vartheta_{\max}(\vartheta_0) \approx \begin{cases} -\vartheta_0 - \left[\frac{R_{\text{sf}}}{L_1 + L_2} (\vartheta_0 - \vartheta^*) \right], & \vartheta_0 \leq \vartheta^*, \\ -\vartheta_0 - \left[\frac{R_{\text{sf}}}{L_1} (\vartheta_0 - \vartheta^*) \right], & \vartheta_0 > \vartheta^*, \end{cases} \quad (30)$$

with the definition $\vartheta^* = \arcsin(a/2R_{\text{sf}}) \approx (a/2R_{\text{sf}})$.

V. COMPARISON OF EXPERIMENT WITH THEORY

A. Diffraction peak intensities

For comparison with theory it is advantageous to analyze relative diffraction intensities that are normalized to the zeroth-order diffraction peak. In this way the need to predict intensities which depend on detector efficiencies and other experimental factors which are difficult to determine absolutely is circumvented. To take into account the broadening of the measured diffraction peaks due to the velocity spread of the atomic beam, the areas of the peaks instead of the heights were evaluated by fitting each diffraction peak to a Gaussian profile as shown in Fig. 6. The areas were then divided by the respective zeroth-order peak area for each angle of inclination to give relative diffraction intensities $i_{n,0}$.

In the first method used to analyze the measured diffraction intensities, Eq. (18), describing the diffraction of a plane wave by an imperfect grating with vanishing thickness, is used. In addition, a perfectly uniform period, $\sigma_d = 0$, is assumed for simplicity with identical Gaussian randomness in the leading and trailing edges of the slits, $\sigma_{s1} = \sigma_{s2} \equiv \sigma$. Then, from Eq. (18) the ratios of the intensity of the n th-order peak to that of the zeroth-order peak are given by the slit function modified by the appropriate Debye-Waller factor

$$i_{n,0} = \frac{I_n}{I_0} = \left[\frac{\sin(n\pi s/d)}{n\pi s/d} \right]^2 \exp[-(2\pi n/d)^2 \sigma^2]. \quad (31)$$

Figure 10 shows some of the data of Fig. 5 plotted as relative diffraction peak areas normalized to the zeroth-order peak area. The curves in Fig. 10 represent least squares fits based

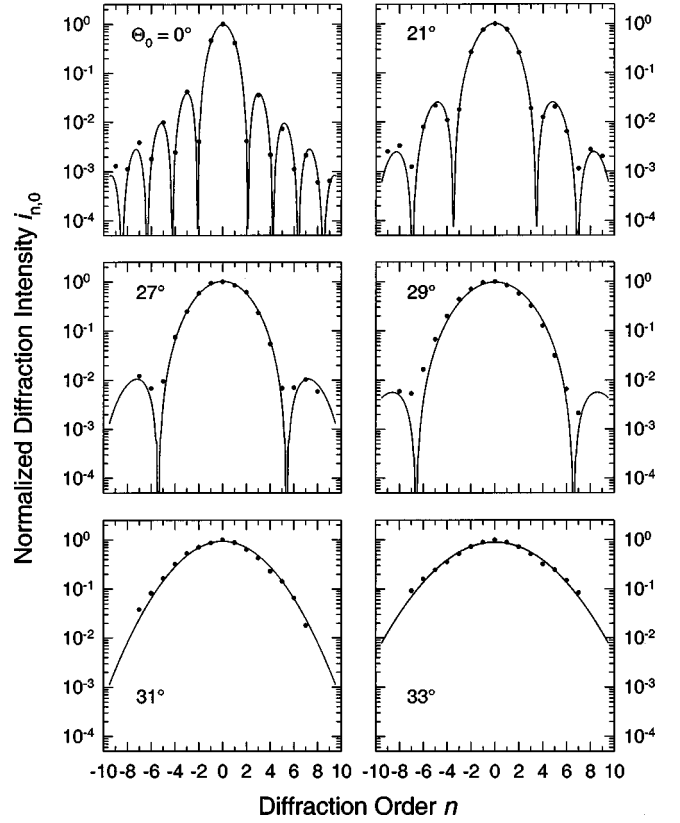


FIG. 10. Experimental diffraction intensities evaluated from the data in Fig. 5 normalized to the respective zeroth-order intensity (filled circles) compared with best fits of the Debye-Waller damped slit function (solid line) of Eq. (31).

on Eq. (31) which yield both the effective slit width s_{eff} and the randomness σ for each angle of inclination. Reasonable fits could only be obtained for angles of inclination smaller than $\Theta_0 \approx 30^\circ$ and the results for both gratings are listed in Table I. The slit width at normal incidence $\Theta_0 = 0^\circ$ is found

TABLE I. Comparison of effective slit widths determined from transmission experiments according to Eq. (1) with those from best fits of the damped slit function according to Eq. (31) for different values of the angle of inclination Θ_0 . Also shown are the best-fit mean square deviations.

Θ_0	Transmission s_{eff} (nm)	Diffraction s_{eff} (nm)	σ (nm)
Grating I:			
0°	47.21	47.21	2.25
21°	25.99	28.87	2.62
27°	13.34	18.54	2.63
29°	9.23	15.17	2.57
Grating II:			
0°	57.34	57.34	2.61
15°	46.11	46.30	2.91
20°	37.75	40.15	2.58
25°	27.95	31.69	3.06
30°	17.68	23.30	2.90

to be $s \approx 47.2$ nm and $s \approx 57.3$ nm for grating I and for grating II, respectively, differing slightly from the nominal value of 50 nm. These values have been used as $s_{\text{eff}}(\Theta_0=0)$ in Eq. (1) to determine the effective slit width as a function of angle of inclination from the measured krypton transmission as shown in Fig. 4. The results are listed in Table I as well. Both the transmission and the diffraction measurements show the decrease of the effective slit width with increasing angle of inclination, but consistently for both gratings the effective slit widths determined from the transmission data decrease faster with increasing angle of inclination than those determined from the diffraction intensities. The large discrepancy especially at large angles of inclination is surprising.¹ Possibly, it is due to an increased deviation of the diffraction intensities from Eq. (31), which is based on Kirchhoff's extinction boundary conditions, which neglect the influence of the van der Waals interaction potential between the ⁴He atom and the grating surfaces. For smaller effective slit widths at larger angles of inclination, this effect, which, in the diffraction of the heavier rare gas atoms has been observed to change the relative diffraction intensities significantly [9], is no longer negligible, and the diffraction patterns are less well described by an effective slit width. This conclusion is confirmed by the fact that for angles of inclination larger than 30° satisfactory fits by Eq. (31) could not be found with reasonable values of the effective slit width indicating the failure of the optical formula Eq. (31). This failure can in part also be attributed to a breakdown in the Gaussian distribution used to mimic the distribution in defects. As discussed in Sec. III in connection with Fig. 5, nonuniformity of the grating edges has an ever increasing effect on the diffraction patterns with increasing Θ_0 .

Deviations from and failure of the optical formula Eq. (31) at large angles of inclination cannot be explained by taking into account that the trapezoidal cross sections of the grating bars are likely to be rounded. Rounded trapezoids would also be described by an effective slit width in combination with possible random disorder, whereas the discrepancy observed at large angles of inclination indicates a deviation from the concept of effective slit width, i.e., from Eqs. (18) and (31).

The fits for $\Theta_0 < 30^\circ$ all give nearly the same value of the root-mean-square deviation of the slit edge position of approximately $\sigma \approx 2.5$ nm for grating I and about 2.8 nm for grating II, without showing a clear trend with increasing

angle of inclination. These values correspond to only 5% of the slit width indicating the high uniformity of the grating structure.

B. Theoretical simulations of the spectra

The second analysis of the diffraction data was based on a complete numerical simulation of the diffraction spectra using the Fresnel formula Eq. (6) averaged over (i) the incoherence of the source as in Eq. (26); (ii) Gaussian distributions in slit edge positions; and (iii) the velocity distribution of the beam using the speed ratio $S=77$ as determined by independent time-of-flight measurements. The sudden freeze radius was determined from Eq. (21), $R_{sf}=0.2S^{3/2}d_0$ [22], where d_0 is the source aperture. In the present case ($d_0=5$ μm) this gives $R_{sf}=0.67$ mm. In addition, a convolution of Eq. (26) with a Heaviside function accounted for the 25 μm wide detector slit (see Fig. 1). In Fig. 11 the measurements (thick solid lines) are compared with the full simulations (thin solid lines) based on Eq. (26) using a slit width s_{eff} and a rms random disorder in slit edge positions σ , both as determined from the simple fit analysis discussed in Sec. V A.

The overall agreement with the experiment is very good up to about the sixth order. Both the intensities and the background are reasonably well reproduced. The discrepancies in the positions are due to experimental errors in the precise position of the detector. At higher orders and at angles of inclination Θ_0 greater than about 30° the increased disorder, surface roughness, and the influence of the atom-surface potential not accounted for in these simulations appear to make large contributions.

To illustrate the effect of disorder the calculations were repeated with the same average over the temporal and spatial incoherence of the extended beam source, Eq. (26), the same s_{eff} but with neglect of disorder, i.e., $\sigma=0$. These results are also shown in Fig. 11 as thin dotted curves. From the comparison it is seen that slit disorder not only reduces the maximum diffraction peak intensities with an increasingly greater relative effect with increasing diffraction order but also increases the diffuse background between the diffraction peaks.

It has already been shown in Fig. 10 that the decrease in maximum peak intensities due to slit disorder agrees rather well with the analytical expression of Eq. (31). Thus, the agreement with the full numerical simulations shown in Fig. 11 indicates that for calculating the maximum diffraction peak intensities the Fresnel corrections are small and the Fraunhofer expressions are adequate.

Recent experiments and calculations for the diffraction of D₂ and heavy rare gases (Ne, Ar, Kr) by the same grating as used here, show a significant effect of the atom-surface interaction potential on the main peak intensities [9]. Since the attractive atom-surface van der Waals potential is significantly stronger than for ⁴He, these effects are much more readily apparent, for example, for krypton than for helium.

Thus, the present experiments demonstrate that for ⁴He atoms the Kirchhoff boundary conditions, and consequently Fresnel and Fraunhofer theory, are quite adequate for small

¹The discrepancy, which, as discussed in the text, is attributed to a combination of effects resulting from the long-range van der Waals forces and grating imperfections, would be expected to be the opposite with the transmission experiments yielding larger slit widths than the diffraction experiments. This is explained by the fact that in the transmission experiments the detector angular aperture is opened up to $\Delta\theta \approx 3.4 \times 10^{-3}$ rad compared to $\Delta\theta \approx 70 \times 10^{-6}$ rad in the diffraction experiments so that atoms scattered through small angles should be collected and effectively transmitted.

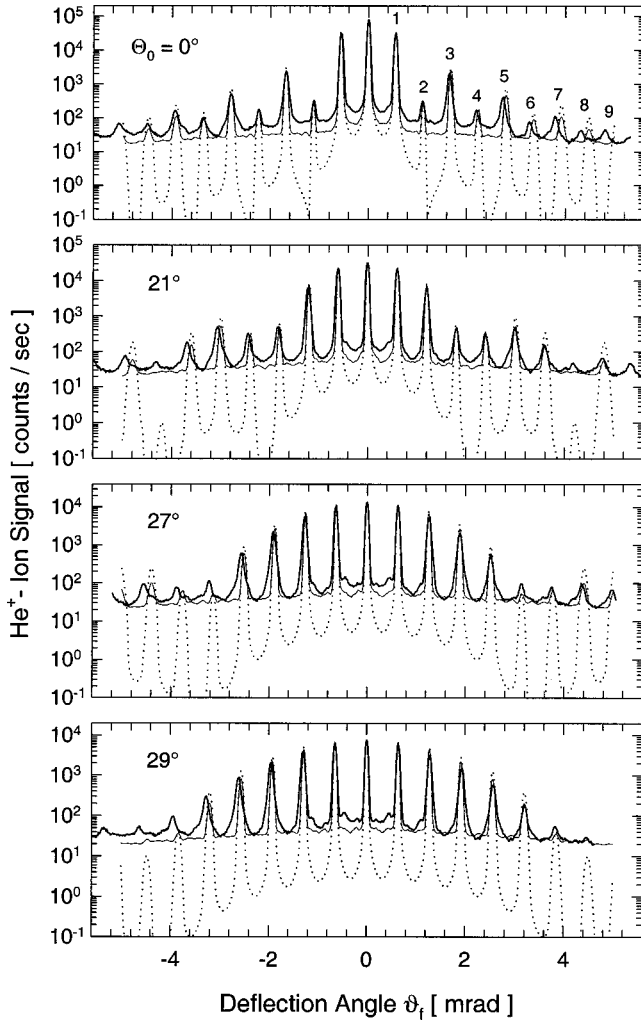


FIG. 11. Full theoretical simulations of the diffraction spectra for several angles of inclination Θ_0 . The thick solid lines represent the experimental results, the thin solid lines the numerical Fresnel calculations of Eq. (26), which include the averages over the incoherence of the extended beam source and the random slit disorder. The thin dotted lines are similar calculations from Eq. (26), but for a diffraction grating without disorder.

diffraction orders and for $\Theta_0 < 30^\circ$, corresponding to effective slit widths $s_{\text{eff}} \geq 9$ nm.

C. Determination of the speed ratio

In addition to providing a detailed characterization of the nanoscale transmission grating as presented in the above sections, the analysis of the diffraction data also provides information on the velocity distribution of the atom beam as is demonstrated in this section.

The width Δv of the atom beam velocity distribution $f(v)$ and hence the speed ratio S can be determined by an analysis of the experimental angular widths $\Delta^{(n)}$ (full widths at half maximum) of the diffraction peaks. The latter is expected to increase monotonically with increasing diffraction order n as a result of the energy spread of the incident beam according to

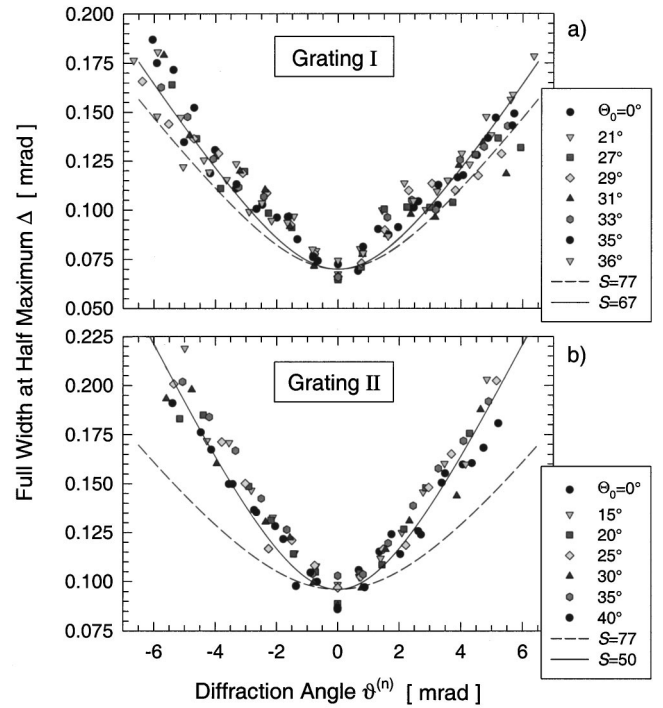


FIG. 12. Widths of the main diffraction peaks (FWHM) for both gratings as extracted from the analysis shown in Fig. 6, plotted against the diffraction angle. The dashed lines represent calculations according to Eq. (32) for a speed ratio of $S=77$, as determined by time-of-flight measurements. Better fits are achieved for $S=67$ and $S=50$ (solid lines).

$$\Delta^{(n)} = \sqrt{(\Delta^{(0)})^2 + \left(\vartheta_f^{(n)} \frac{\Delta v}{u}\right)^2}, \quad (32)$$

where u denotes the mean velocity. This equation is derived from an evaluation of Eq. (26) by assuming Gaussian shapes for both $f(v)$ as well as the zeroth diffraction order of angular width $\Delta^{(0)}$, which is determined by the beam divergence through the collimating slits and the spatial extent of the beam source as described above. It follows that a measurement of the increase in diffraction peak widths provides an independent measurement of the speed ratio S of the incident beam, in addition to the direct time-of-flight (TOF) measurements of S .

Figure 12 shows a plot of the FWHM of the Gaussians fitted to the main diffraction peaks as in Fig. 6 as a function of diffraction angle. For comparison the dashed lines represent the theoretical widths as given by Eq. (32) in which a speed ratio equal to the value $S=77$ measured by TOF was assumed. In Fig. 12(a) (grating I) a slightly better fit of the data is achieved if $S=67$ is assumed (solid line). In Fig. 12(b), where the data for the newer grating (grating II) is plotted, a better fit is obtained for $S=50$ (solid line). Whereas the grating I value agrees quite well with the TOF result, grating II shows a significant discrepancy. This disagreement appears to be only apparent. Since the ghost peaks are much less pronounced and less well resolved as compared to grating I, it was not meaningful to use extra Gaussians to fit the small ghost peaks in all of the diffraction

TABLE II. Summary of the properties of two 100 nm-period transmission gratings obtained from He atom diffraction and transmission experiments, which were analyzed following procedures described in this paper.

	Slit width ($\Theta_0=0^\circ$) s (nm)	Bar profile wedge angle α ($^\circ$)	Bar thickness t (nm)	Randomness of
				slit edge positions σ (nm)
Grating I	47.21	7.5 ± 1.5	90 ± 10	2.25
Grating II	57.34	8.0 ± 1.5	90 ± 10	2.61

peaks. The neglect of additional Gaussians results in an overestimation of the widths of the main diffraction peaks and can explain the discrepancy.

VI. CONCLUSIONS

In the present work ^4He atom diffraction has been used to characterize the structural features and imperfections of 100 nm-period transmission gratings used in atom and cluster beam diffraction experiments [3]. The results show clearly that the simple Kirchhoff formula commonly used for optical scattering is only able to qualitatively describe the measured diffraction spectra. In the course of the present studies the average slit width, the actual profile and thickness of the bars, and the statistical randomness in the bar edge positions of two gratings were determined. The results for the gratings studied are summarized in Table II.

The slit widths are determined by a best fit of the diffraction intensities which depend sensitively on the ratio of the effective slit widths to the bar widths, but also to a lesser extent on the distribution of the bar edge positions. A simple theory, which provides a convenient approximation to account for the randomness in the bar edge positions, is derived based on the analogy to the well-known Debye-Waller factor.

The profiles and effective thickness of the grating bars were simply determined by measuring the dependence of the overall transmission of the grating as a function of the angle of inclination of the grating with respect to the incident beam direction. By inclining the grating with respect to the incoming atomic beam, the effective slit widths are decreased and the deviations from the ideal Kirchhoff behavior become increasingly important. Under these conditions the random variations of the slit width constitute an increasingly larger fraction of the effective slit width and their effect become increasingly apparent. The diffraction patterns measured for different angles of inclination reveal a number of additional periodic structures which are especially apparent near the central peak and with increasing angle of inclination. These have been tentatively assigned to Lyman ghosts since they appear to be correlated with structural imperfections.

To obtain a full simulation of the measured diffraction

pattern the finite velocity spread and spatial extent of the beam source also had to be accounted for. When all these effects are included a very satisfactory fit of the data out to intermediate diffraction orders ($n \leq 6$) and at not-too-large angles of inclination was achieved.

The experience gained here and the procedures developed are an important prerequisite for many applications of diffraction gratings for physical investigations. They confirm the previous interpretation of satellite structures obtained at lower source temperatures ($T_0 \leq 50$ K) in terms of small He clusters [3,5] and help delineate conditions under which spurious effects may be expected and discounted in future studies. Recently, large differences have been found in the relative intensities of different diffraction orders in experiments with room-temperature supersonic atomic beams of He, Ne, Ar, Kr, and D_2 [9]. In order to relate these observations to the effect of the long-range C_3/z^3 attractive potential between the atoms and the grating bars the grating imperfections studied here all have to be correctly accounted for. Another application aims at determining the mean internuclear distances of the He dimer and trimer. Because of their large physical size the effective slit widths are expected to be reduced as compared to the diffraction of He atoms, and this effect will also lead to changes in the relative intensities at the different diffraction orders [24]. In this case to determine the effective slit width all the above imperfections as well as the effect of the long-range potential must be properly accounted for.

We hope that this investigation will stimulate the further development of the technology of fabricating transmission gratings and their widespread use in molecular and atomic physics.

ACKNOWLEDGMENTS

We thank G. C. Hegerfeldt and T. Köhler for many fruitful discussions about the role played by the van der Waals interaction potential in diffraction experiments. J.R.M. would like to thank the Max-Planck-Institut für Strömungsforschung for hospitality during the course of this work, and would like to acknowledge support by the NSF under Grant No. DMR-9726229.

APPENDIX

The fabrication of grating I used a bilayer-resist process [25] followed by evaporation of titanium on the tops of resist lines. In the process of etching through the antireflection layer and the SiN_x , thermally induced stress in the Ti caused some of the grating bars to deviate. In some cases adjacent bars approached one another. We believe this is probably the origin of the Lyman ghosts. To avoid this problem, a trilayer-resist process was developed and used to fabricate grating II. No evidence of deviations was observed with the trilayer process, which is consistent with the near absence of the ghosts that were observed with grating I.

- [1] *Atom Interferometry*, edited by P. R. Berman (Academic Press, New York, 1997).
- [2] D. W. Keith, M. L. Schattenburg, H. I. Smith, and D. E. Pritchard, *Phys. Rev. Lett.* **61**, 1580 (1988).
- [3] W. Schöllkopf and J. P. Toennies, *Science* **266**, 1345 (1994).
- [4] O. Carnal, A. Faulstich, and J. Mlynek, *Appl. Phys. B: Photophys. Laser Chem.* **53**, 88 (1991).
- [5] W. Schöllkopf and J. P. Toennies, *J. Chem. Phys.* **104**, 1155 (1996).
- [6] F. Luo *et al.*, *J. Chem. Phys.* **98**, 9687 (1993).
- [7] R. E. Grisenti, W. Schöllkopf, J. P. Toennies, G. C. Hegerfeldt, and T. Köhler (unpublished).
- [8] M. Born and E. Wolf, *Principles of Optics* (Pergamon Press, London, 1975).
- [9] R. E. Grisenti, W. Schöllkopf, J. P. Toennies, G. C. Hegerfeldt, and T. Köhler, *Phys. Rev. Lett.* **83**, 1755 (1999).
- [10] T. Lyman, *Phys. Rev.* **12**, 1 (1901).
- [11] R. W. Wood, *Philos. Mag.* **48**, 487 (1924).
- [12] H. G. Gale, *Astrophys. J.* **85**, 49 (1937).
- [13] W. Schöllkopf, J. P. Toennies, T. A. Savas, and H. I. Smith, *J. Chem. Phys.* **109**, 9252 (1998).
- [14] T. A. Savas, M. L. Schattenburg, J. M. Carter, and H. I. Smith, *J. Vac. Sci. Technol. B* **14**, 4167 (1996).
- [15] The definition of the effective slit width given in Fig. 4 differs from the one in Ref. [13] by the factor $\cos \Theta_0$.
- [16] R. E. Grisenti, S. Spuddig, and J. P. Toennies (unpublished).
- [17] M. C. Hutley, *Diffraction Gratings* (Academic Press, London, 1982).
- [18] J. R. Manson, *Phys. Rev. B* **43**, 6924 (1991).
- [19] J. R. Manson, in *Helium Atom Scattering from Surfaces*, edited by E. Hulpke (Springer-Verlag, Berlin, 1992).
- [20] D. E. Miller, in *Atomic and Molecular Beam Methods*, edited by G. Scoles (Oxford University Press, Oxford, 1988).
- [21] H. C. W. Beijerinck and N. F. Verster, *Physica C* **111**, 327 (1981).
- [22] E. L. Knuth (private communication).
- [23] J. P. Toennies and K. Winkelmann, *J. Chem. Phys.* **66**, 3965 (1977).
- [24] G. C. Hegerfeldt and T. Köhler, *Phys. Rev. A* **57**, 2021 (1998).
- [25] T. A. Savas *et al.*, *J. Vac. Sci. Technol. B* **13**, 2732 (1995).